Development of the Onboard Calibration Target for the Arctic Weather Satellite

Roland Albers, Tobias Plüss, *Member, IEEE*, Lars Eggimann, and Axel Murk

***Abstract*— We present the design and characterization of the onboard calibration target (OBCT) for the arctic weather Satellite radiometer. The arctic weather satellite (AWS) is a single-instrument mission consisting of a cross-track scanning microwave radiometer. The radiometer optics consists of a feed cluster with four horns (54, 89, 183, and 325 GHz) directly illuminating a primary scanning mirror. The OBCT is a wedge-shaped cavity with an absorber consisting of an epoxy-based mixture, developed and produced by the University of Bern. The coupling into the target via a secondary mirror is simulated using Ticra Tools and the effects of the divergent beams are investigated. We present the development of the target and laboratory measurements of the flight model showing a return loss of 55 dB or better for all bands in TM mode. A worst case thermal simulation is presented, highlighting possible temperature gradients in the target.**

***Index Terms*— Absorber, blackbody, mm-wave, radiometer, remote sensing.**

I. Introduction

OBSERVATIONS from space-based microwave radiometers are a crucial component of global weather forecasting. Several national or international meteorological services operate their own satellites which include microwave radiometers, typically with decade-long service lives. To maintain accurate measurements, the microwave sounders need to be calibrated continuously, as gain variations in the receiver can occur on a second timescale. This is typically achieved by two-point calibration, using "cold" deep space measurements in combination with a "warm" onboard calibration target (OBCT), where the OBCT is made up of a periodic array of pyramidal elements. Such a target is used by all major meteorological operators such as metop second-generation (Metop-SG) [1], joint polar satellite system (JPSS) [2], and Fengyan-3 (FY-3) [3]. The pyramidal elements exploit multiple reflections between them to increase the return loss of the OBCT. They also offer consistent performance for both linear polarizations, which enables using polarizing grids to co-align beams in the quasi-optics. Another polarization agnostic option is a conical OBCT which is, for example, used in the submillimeter-wave instrument (SWI) on the Jupiter icy moons explorer (JUICE) [4], because the two bands' ($\sim$ 600 and $\sim$ 1100 GHz) polarizations are orthogonal. A cone requires a larger volume for equivalent aperture than an array of pyramids, but since the SWI bands measure at much higher frequencies (shorter wavelength) than for Met-OP, JPSS, and FY-3, it could be accommodated. In general, the main drawback of including an OBCT is the required additional mass and volume, but since these microwave sounders are part of a suite of instruments hosted on a large satellite platform this is permissible. On some CubeSat missions such as the 3U TROPICS constellation [5] where including an OBCT is not possible, noise diodes are used to generate a calibration source electrically, which is injected at the input of the receiver chain. However, one disadvantage of this method versus using an OBCT is that it cannot remove errors introduced by the quasi-optics such as reflector spillover. Other CubeSat missions such as TEMPEST-D [6] do include an OBCT for continuous calibration by scaling up to 6U. However, due to the limited volume, the OBCT size and positioning are restricted. This affects the number of usable samples and possible thermal gradients across the OBCT. The size of the arctic weather satellite (AWS) mission is in between these programs as a single payload mission with a cross-track scanning microwave radiometer, built by AAC Omnisys on a SmallSat platform from OHB Sweden. It is a prototype for a constellation of operational microwave sounders called EUMETSAT Polar System (EPS) Sterna. The constellation will consist of six satellites, improving global numerical weather prediction and providing frequent revisit times [7]. It uses four bands (54, 89, 183, and 325 GHz) with a total of 19 channels to retrieve temperature and water vapor profiles, as well as cloud liquid water content and precipitation. Since the AWS is designed with a constellation in mind, it is constrained in volume, cost, and complexity to keep building up to 20 copies affordable. Regarding quasi-optics, this is achieved by forgoing beam co-alignment and, consequently, any additional components typically needed, such as mirrors, dichroics, and polarizing grids. A split-block feed cluster with four horns directly illuminates the continuously rotating primary mirror. Since all the bands share one polarization, the OBCT is wedge-shaped. A wedge is simpler to manufacture, but offers optimal performance for only one polarization. To reduce the OBCT aperture size and hence its volume, a second mirror is used to refocus the beams. This article presents the development, simulation, and measurements of the OBCT.

II. Optics

A distinguishing feature of the AWS optics is the split-block feed cluster which illuminates the primary scanning mirror without any beam co-alignment. The scanning mirror is

Manuscript received 1 March 2024; revised 24 June 2024 and 24 July 2024; accepted 27 July 2024. Date of publication 1 August 2024; date of current version 15 August 2024. *(Corresponding author: Roland Albers.)*

The authors are with the Institute of Applied Physics, Bern University, 3012 Bern, Switzerland (e-mail: roland.albers@unibe.ch).

Digital Object Identifier 10.1109/TGRS.2024.3436517

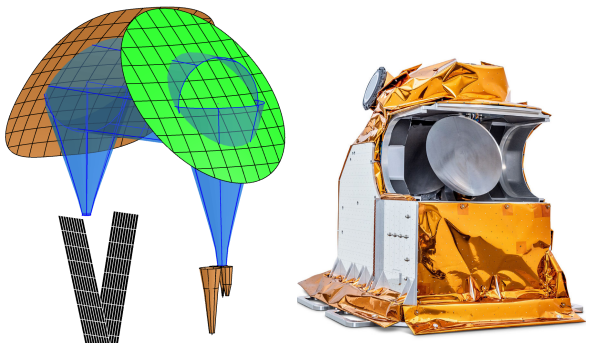

Fig. 1. Picture of relevant elements for OBCT simulation in Ticra Tools (left). Primary mirror (green) shown in zenith scan position, focusing mirror in orange, OBCT absorber surface in black. 20-dB Gaussian beam tube of 183-GHz feed for visualization only. Picture of AWS OBCT PFM (right), courtesy of AAC Omnisys. Approximate instrument size: 390 × 660 × 540 mm.

an offset parabolic mirror, rotating continuously at 0.84 Hz. Although the overall optics are simpler and more compact in this configuration compared with quasi-optical networks which include elements for co-alignment, the effect of each feed's lateral offset from the focal axis of the reflector in the feed cluster plane needs to be considered. Most importantly, the beams diverge from the outgoing focal axis of the reflector and rotate around it as a function of scan angle. A detailed assessment with regard to spillover, beam far-field performance, and optimization can be found in [8]. The primary scan mirror couples into the OBCT through a fixed parabolic mirror positioned in zenith. Both the mirrors consist of machined aluminum. The focusing mirror fills a minimum of 10° in the rotation of the primary mirror (Fig. 1). However, the exact position of this arc in the rotation of the primary mirror varies for each feed horn, due to the aforementioned beam divergence. Furthermore, the beams do not track across the OBCT aperture in a straight line, but in a curve due to their rotation around the reflector focal axis. Fig. 2 shows the track of each beam across the aperture of the OBCT as a superposition of 30-dB contours. The apex of the wedge is marked by the vertical dotted line dividing the aperture outline. It is also apparent that due to the beam divergence, each beam is illuminating different parts of the OBCT aperture. Furthermore, the sizes of the contours differ between channels, due to the different directivities of each horn. For a given scan angle, the 325-GHz band will illuminate a much smaller section of the wedge than the 52-GHz band. This should be considered if there are temperature gradients in the OBCT during operational use. Fig. 3 shows a comparison of the coupling into the OBCT aperture for each beam (dashed line) against a test measurement of the protoflight model (PFM). During normal operation, the scan range across the OBCT is only 10.6° over 15 samples, avoiding recording unnecessary data. The dataset shown here has a larger range, which is useful to compare the simulated coupling into the OBCT aperture with the as-built configuration. The measurement was taken in atmosphere while a liquid nitrogen (LN2) target was positioned in the nadir view of the instrument, making the OBCT the hottest object in view of the instrument. OBCT temperature data were also recorded during this test and used to scale the

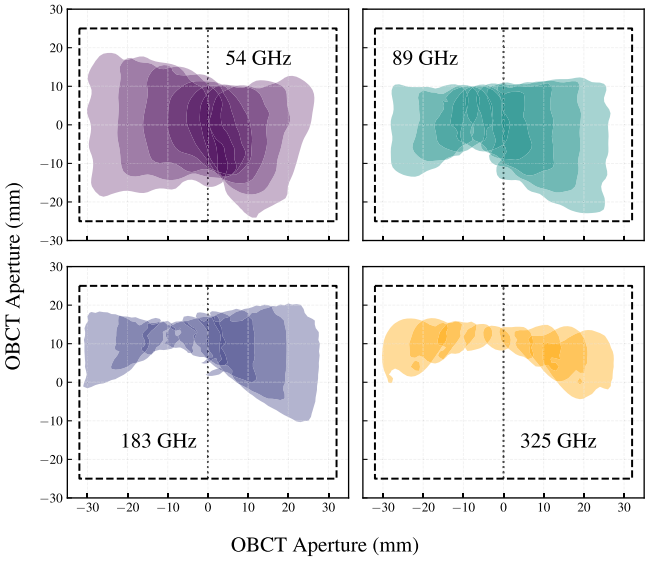

Fig. 2. Coverage of each beam as they track over the OBCT aperture (dashed line), shown as superposition of 30-dB contours for individual scan angles.

recorded counts. The measured counts have been calibrated by taking the typical Y-factor from other measurements and subtracting a system noise temperature for each channel so that the highest count value is equivalent to the peak temperature measured for the OBCT (302.4 K). While this is not a proper calibration, it converts the raw count data of each channel into a common and comparable scale. The gray area denotes the scan angle range where the coupling is equal or larger than 99%, which is larger than the required 10° for all beams. The 99% coupling factor does not consider the spillover occurring at the primary mirror. It refers only to the possible spillover at the calibration mirror and OBCT aperture. All the channels show temperature decreases when coupling decreases, since the fact that the AWS and its restricted viewport are metal causes any reflections to predominately view the LN2 target. The slope of the coupling decrease is a function of beam size and increases in steepness with frequency.

III. Onboard Calibration Target

The AWS OBCT consists of a wedge-shaped cavity with a rectangular aperture (Fig. 4). Aluminum backing plates hold the in-house developed absorber based on epoxy resin. Each backing plate is equipped with four resistance temperature detectors (RTDs) cast into the weight saving pockets on the back of the plates. A total of eight RTDs form two redundant sets of temperature sensors across both the wedge sides. Two thin aluminum plates with thermally absorbing paint close the wedge at either side. They are electrically reflective and do not contribute to the absorption of the OBCT. Two thick aluminum plates provide structural support and form the interface to the instrument base plate. They are gold-plated to minimize radiative thermal coupling with surrounding components, which could induce a temperature gradient across the OBCT. The OBCT is entirely passive and does not include any capability to control its temperature. The OBCT fits inside a footprint of 170 × 110 mm with a height of 163 mm and weighs just

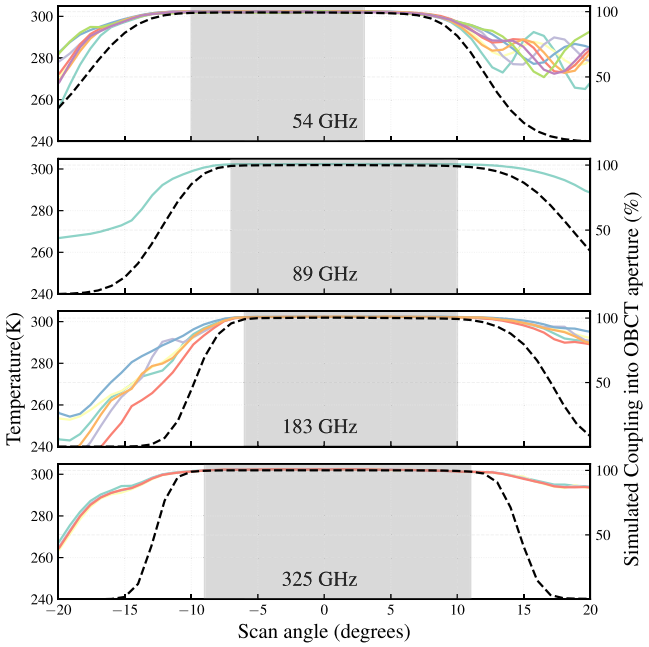

Fig. 3. Simulated coupling into the OBCT aperture (dashed lines) against measured brightness temperature on the PFM instrument (colored lines). The gray area denotes coupling $\geq$ 99%. Spillover at the primary mirror is not considered. Scan angles are relative to zenith position.

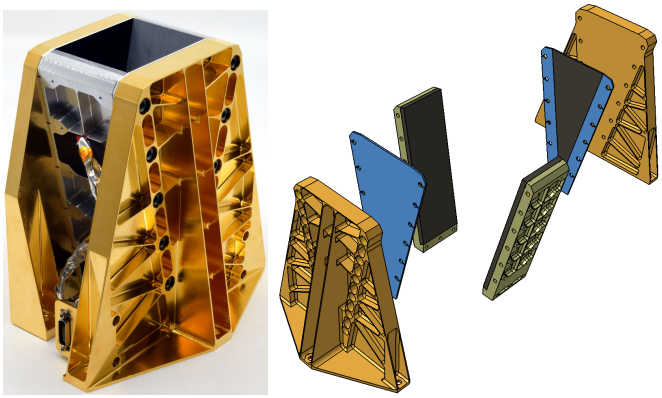

Fig. 4. Picture of assembled AWS OBCT (left). Exploded view on the right. The OBCT fits inside a 170 × 110 × 163 mm volume and weighs slightly less than 1 kg.

under 1 kg. The return loss requirement for the OBCT is 50 dB or better to minimize coherent backscatter inducing standing waves.

A. Absorber

As part of the Metop-SG program, other epoxy-based absorber mixtures have been developed at the University of Bern [9]. The Metop-SG absorber consisted of Stycast 2850FT mixed with carbonyl iron powder (CIP). Using a magnetic material was necessary to achieve the required absorption at the low end of the Metop-SG Microwave Sounder bands (23.8 and 31.4 GHz). The downside of the previous mixture is the high refractive index of Stycast 2850FT ($\epsilon_r > 5$) which increases with CIP loading. Low reflectivity is desirable as it enables higher absorption for the same number of reflections. Since the lowest AWS band starts at 50 GHz, it is possible

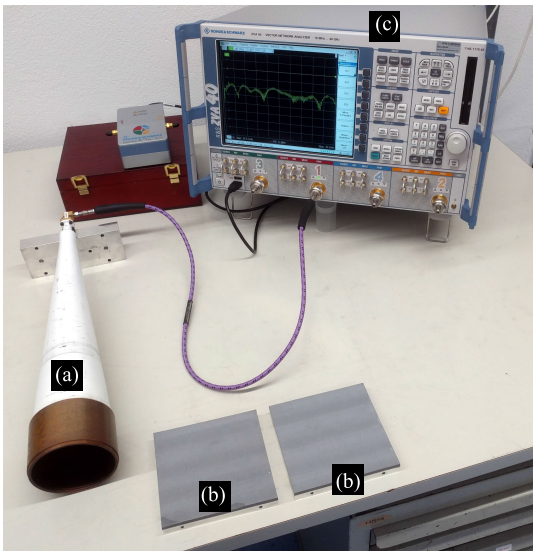

Fig. 5. Return loss measurement of absorber breadboard. (a) Ka-band corrugated horn antenna. (b) Material samples to be tested. (c) Rohde & Schwarz ZVA40 network analyzer.

to use other absorbing materials which are assumed to be nonmagnetic. Another downside of Stycast 2850FT in our experience is that a high concentration of absorber material mixed into the epoxy leads to difficulty in manufacturing due to the high viscosity. Finally, there is an issue with poor thermal conductivity of the absorber mixture, increasing potential temperature inhomogeneities between the temperature sensor in the aluminum backing plate and the epoxy, where absorption occurs. Consequently, another absorber mixture was developed with the aim of addressing the aforementioned issues. It consists of three parts, Stycast 1266 ($\epsilon_r = 3$) as the epoxy base, carbon black powder as the absorbing additive, and boron nitride as thermal conductivity influencing additive. Boron nitride is a common insulating additive for epoxies and often used to produce thermal paste among other applications.

Several iterations of absorber mixture were cast as breadboards. Using a vector network analyzer (VNA), the return loss of each sample was measured from 27 to 40 GHz, which is the upper limit of the VNA (Fig. 5) without extensions. The measurements were taken with the absorber layer contacted against the aperture of the horn and calibrated with a second measurement of the metal backing face, serving as a perfect reflector.

Fig. 6 shows return loss measurements of two breadboards with identical absorber mixtures, demonstrating good repeatability of the manufacturing process. The ripple on the measurements is caused by standing waves inside the horn antenna. Using these measurements, the relative permittivity of the absorber material can be determined using a nonlinear fitting procedure as follows.

The return loss of the samples is described by

$$S_{11} = \frac{\Gamma - z^2}{1 - \Gamma z^2} \tag{1}$$

where

$$\Gamma = \frac{\sqrt{\frac{1}{\hat{\epsilon}_r}} - 1}{\sqrt{\frac{1}{\hat{\epsilon}_r}} + 1} \tag{2}$$

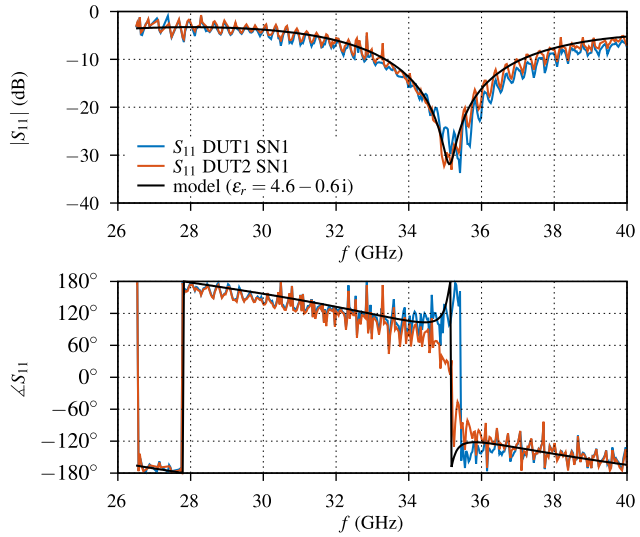

Fig. 6. S_{11} measurements of two breadboards with identical absorber.

is the reflection coefficient at the surface of the absorber layer, and

$$z = \exp\left(-\mathrm{i}\frac{\omega}{c}\sqrt{\hat{\epsilon}_r}\, d\right) \tag{3}$$

is the transmission coefficient inside the absorber and d is the material thickness [10], [11]. Finally, using

$$\hat{\epsilon}_r = \arg\min \left| S_{11,\text{measured}}(f) - S_{11,\text{calculated}}\left(f, \hat{\epsilon}_r\right) \right| \tag{4}$$

yields the relative permittivity used for the calculated return loss plot seen in Fig. 6. We assume the permittivity to be constant over the frequency range of our measurement to the top end of the AWS range.

With this assumption, using an in-house 2-D plane-wave tool, a simulation of the expected return loss for a wedge with a 12° opening angle and various thicknesses can be generated (Fig. 7). The simulation takes both transverse electric (TE) and transverse magnetic (TM) incidence into account. TE means that the electric field is polarized parallel to the apex of the wedge, whereas TM means that the electric field is polarized perpendicular to the apex. At lower frequencies, the return loss oscillates, as it depends on the constructive or destructive interference of the reflections at the air/absorber and absorber/metal interfaces. As the thickness increases, absorption inside the material dominates and the ripple disappears. The vertical solid white lines mark the centers of each AWS frequency band. The horizontal solid white lines indicate potential absorber thicknesses which provide return loss below 50 dB in the relevant bands. For the final wedge, an absorber thickness of 3.5 mm was chosen as a compromise between maximizing performance and minimizing mass.

B. Performance

The OBCT return loss (S_{11}) was measured in the lower three AWS frequency bands (54, 89, and 183 GHz). Due to lack of available hardware, the 325-GHz band measurement was replaced by a measurement at 400 GHz. Since the predicted performance of the OBCT is relatively constant above

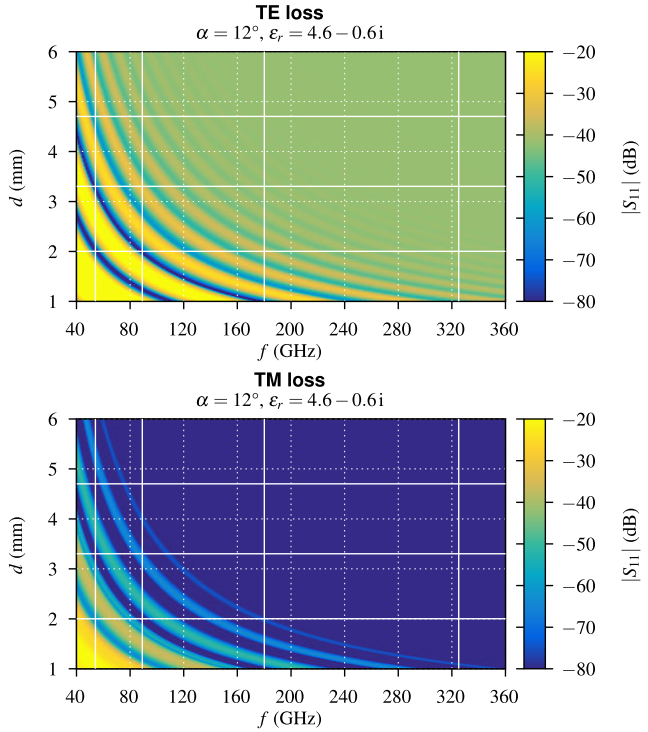

Fig. 7. Simulated return loss against thickness and frequency of the final absorber mixture for both the polarizations.

200 GHz, there should be no significant difference between these two bands. The measurements were performed prior to integration, without using the feed cluster of the instrument. Instead, each band was measured individually using corrugated feed horns aiming at the center of the OBCT aperture. Consequently, the beam size and positioning within the aperture were not identical to the final use case. For 54 and 89 GHz, a directional coupler was used in combination with the ABmm VNA and appropriate multipliers. Using a translation stage, the OBCT was moved along the symmetry axis of the feed, changing the phase of the backscatter. An identical method was performed using a metal plate instead of the OBCT which was also moved on the translation stage to perform a sliding load calibration. The test setup for 89 GHz is shown in Fig. 8. For 183 and 400 GHz, the directional coupler was replaced by a quasi-optical setup, shown in Fig. 9. More details of the measurement methodology, including the quasi-optical setup for 183 GHz and above, can be found in [9]. As simulations predicted the 54-GHz band to be the most critical, the OBCT was measured in TE, TM, and 45° polarizations (Fig. 10). The OBCT performance is below the targeted return loss of 50 dB for TM and 45° and slightly exceeding it for TE at the high end of the band. A summary of measurement results across all the bands is shown in Fig. 11. As predicted in the simulations (Fig. 7), the TM return loss is lower than for TE. Furthermore, despite assuming constant permittivity, the return loss minimum at the 54-GHz band was measured as predicted.

C. Thermal Error Sources

Aside from the optical aspects, the uncertainty of the OBCT temperature and its homogeneity drives the accuracy of AWS

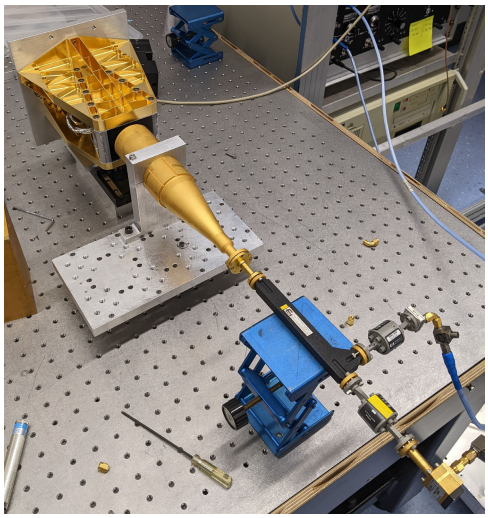

Fig. 8. AWS OBCT return loss measurement setup for 89 GHz.

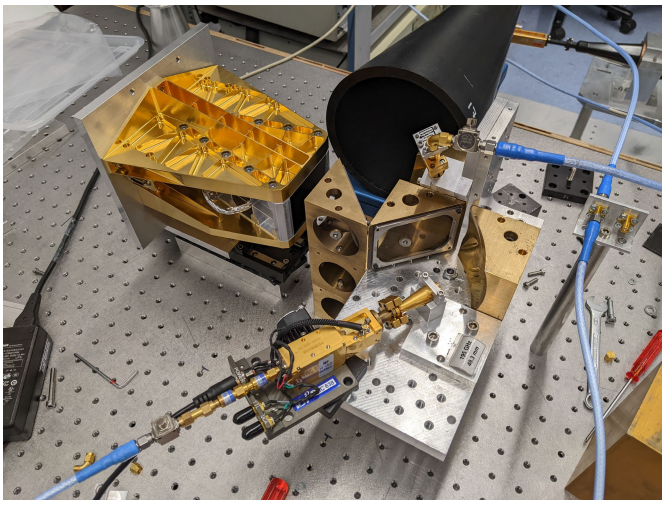

Fig. 9. AWS OBCT return loss measurement setup for 183 and 400 GHz using quasi-optical directional coupler.

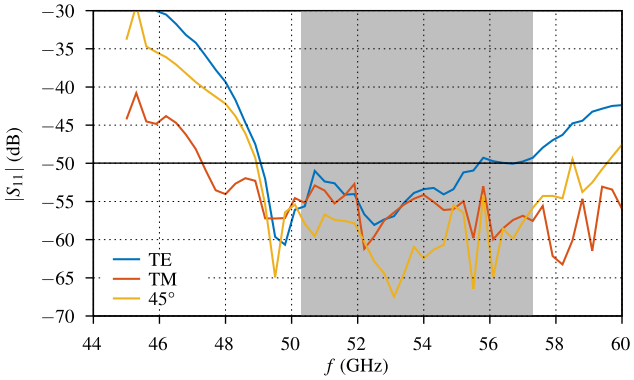

Fig. 10. Measured return loss of AWS OBCT when rotated.

calibration. There are three factors to consider for the OBCT temperature. First, the accuracy of the RTDs themselves causes an error on calibration. For the AWS OBCT, the RTDs were procured according to tolerance class F of the international standard IEC60751. The standard states a tolerance of $\pm 0.15 + 0.002|t|$ where t is the temperature modulus in degree Celsius. The expected operating temperature of the

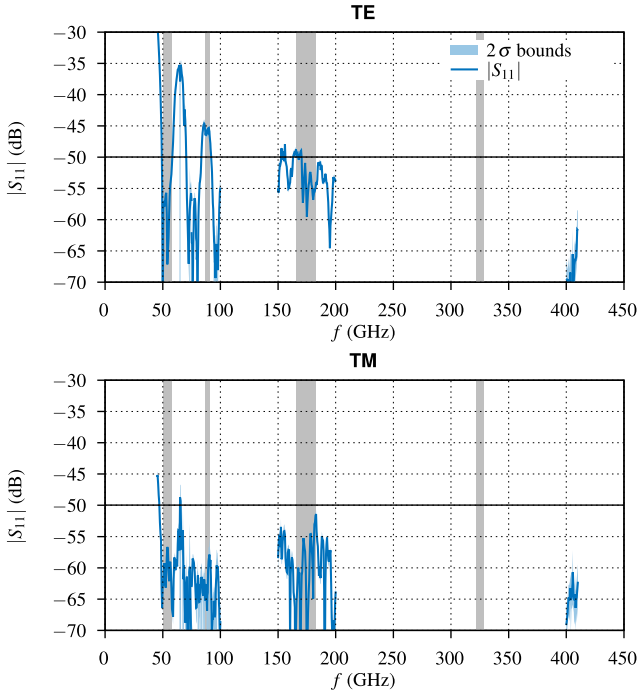

Fig. 11. Measured return loss of AWS OBCT for horizontal and vertical polarizations.

radiometer is approximately 20 °C. Second, as can be seen in Fig. 2, the beams scan across the OBCT aperture, which means they are absorbed—at least for the primary incidence—at different sections of the wedge, depending on the frequency and scan angle. The different wedge sections can vary in temperature both horizontally and vertically. Due to the tall structure of the OBCT and being thermally clamped to the base plate and thermally "floating" at the top, vertical temperature gradients will dominate over horizontal gradients. To resolve these potential gradients, RTDs are located at two heights along the back of the wedge (Fig. 12). Furthermore, the RTDs are split into a nominal (set A) and redundant (set B) set of four. During normal operation, only one set will be read to retrieve OBCT temperature. The distribution shown in Fig. 12 was chosen to enable either set to resolve potential vertical and horizontal gradients independently. However, since the RTDs are located at the back of the aluminum plates and not in the absorber, as this would negatively affect absorption, there will be a difference between the temperature of the absorber and the RTD reading. This gradient is mitigated by maximizing the thermal conduction of the absorber (see Section III-A) and minimizing the thickness of the aluminum and absorber.

A further complication is that the depth at which the radiation is absorbed is frequency-dependent. Consequently, each AWS beam is biased differently by the temperature gradient through the absorber thickness. As a worst case scenario, the minimum absorption path is twice the absorber thickness or 7 mm, which is equivalent to perpendicular incidence. However, for the first reflection the incidence is very shallow. When the primary mirror is in the zenith position and coupling into the center of the OBCT aperture, the angle of incidence is half the wedge apex angle or 12° for the mirror boresight. This

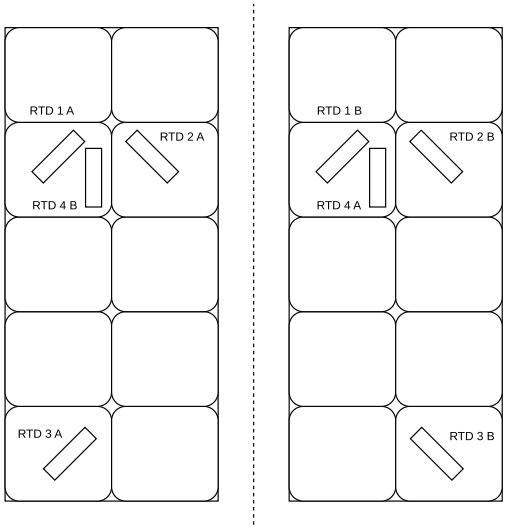

Fig. 12. Schematic of both AWS backing plates and their RTD distribution.

is the same incidence as during the return loss measurements shown in Figs. 8 and 9. However, since the absorber is a lossy material, the incident beams will be refracted [12]. The angle of transmission is

$$\chi_2 = \tan^{-1}\left[\frac{\sqrt{2}k_1 \sin\theta_1}{\sqrt{\sqrt{p^2+q^2}+q}}\right] \tag{5}$$

where k_1 is the wavenumber in free space, and θ_1 the angle of incidence. The abbreviations p and q are

$$p = 2\alpha_2\beta_2, \quad q = \beta_2^2 - \alpha_2^2 - k_1^2 \sin^2\theta_1 \tag{6}$$

where α_2 and β_2 are the absorber's attenuation constant and phase constant, respectively, as follows:

$$\alpha = k_1\sqrt{\frac{\epsilon_r'}{2}\left(\sqrt{1+\frac{\epsilon_r''^2}{\epsilon_r'}}-1\right)} \tag{7}$$

and

$$\beta = k_1\sqrt{\frac{\epsilon_r'}{2}\left(\sqrt{1+\frac{\epsilon_r''^2}{\epsilon_r'}}+1\right)}. \tag{8}$$

Assuming a constant permittivity ϵ for all frequency bands, the angle of transmission is 24.5° for all bands. This increases the worst case absorption path by a factor of $(1/\cos(24.5°)) = 1.09$. The beam divergence of the bands due to the feed offset is not considered, which puts them 1°–2° off the mirror boresight. At each reflection, a fraction of the beam intensity will be transmitted into the absorber. The skin depth δ_s defines the depth at which the electric field of a wave of a given frequency has decayed by a factor of 1/e and is given by [12]

$$\delta_s = \frac{1}{\alpha}. \tag{9}$$

This is equivalent to a power fraction of $1/e^2 \approx 14\%$, which is not large enough to make a judgment on whether and where in the absorber material the transmitted beam is sufficiently attenuated. $2.5\,\delta_s \approx 1\%$ is calculated to represent a more intuitive value

Frequency (GHz)	54	89	183	325
$2.5\,\delta_s$ (mm)	15.8	9.6	4.7	2.6

(10)

In the worst case scenario of perpendicular incidence (7-mm absorption path), only the 183-and 325-GHz bands meet the defined absorption threshold of 1%. At first reflection conditions with an absorption path of $1.09 \times 7\,\text{mm} = 7.63\,\text{mm}$, the other bands are still not sufficiently attenuated. Nevertheless, as absorption occurs deep in the material and after reflecting off the metal backing plate, a vertical temperature gradient in the absorber will affect all the four bands. Apart from the 183-and 325-GHz band, the beams will not attenuate sufficiently at first incidence and the energy transmitted into the absorber will propagate further into the wedge.

IV. OBCT Thermal Simulation

To gain an appreciation of the possible thermal gradients of OBCT during operation, thermal simulations were performed using the ANSYS thermal analysis software. A CAD model of the OBCT was imported and thermally clamped to a simplified base plate at a temperature of 35 °C. The environment was set at −10 °C, which is equivalent to a homogeneous minimum operating temperature of the instrument structure. This particular combination of temperatures represents the worst case condition during operation of the instrument. As the OBCT sits deep within the structure which is covered in multilayer insulation (MLI), it is assumed to be unaffected by thermal radiation external to the instrument, e.g., from the Earth or sun. The crescent-shaped shield seen on the right of the instrument in Fig. 4 offers further protection from direct sun intrusion. Emissivity measurements of the absorber material at infrared wavelengths are not available, and therefore the assumed value is 1 as a worst case value. The aluminum and gold plating of the OBCT have emissivities of 0.1 and 0.025, respectively [13].

Fig. 13 shows the extracted temperature profile along the vertical axis of the OBCT (upward direction in Fig. 4) for three different locations along the absorber backing plates. The x-axis shows the vertical distance from the bottom wedge up toward the wedge opening. The solid blue line denotes the temperature profile along the surface of the absorber. The dashed line is for the same horizontal location at the interface between the absorber and the aluminum backing plate holding it. The dotted line corresponds to the temperature along the backside of the aluminum backing plate, where the temperature sensors are located. The temperature profile is not an average of the whole plate but taken at the center line of the pockets on the back of the plate. Each line starts at a different z position, according to the vertical height at which the feature they represent begins. The crosses denote the positions where the RTDs are located.

Since the surroundings are at a lower temperature than the baseplate, the temperature decreases with distance from the base plate, as expected. The larger drop toward the wedge aperture in absorber temperature can be explained by the exponentially increasing viewing angle to the cold surrounding

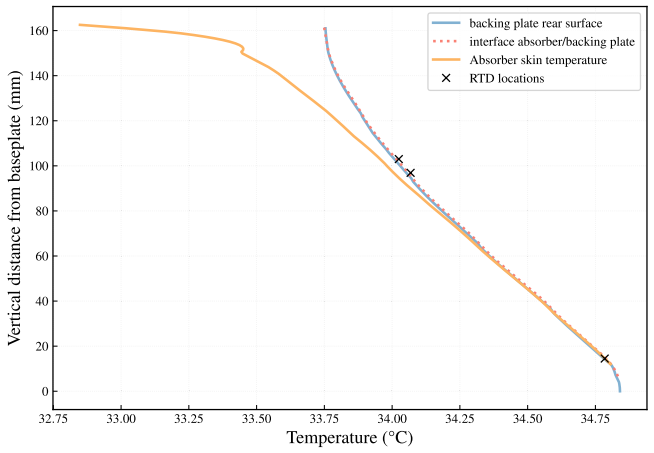

Fig. 13. Simulated temperature of OBCT absorber and its backing plate for minimum operating temperature.

and the high absorber emissivity. The wedge temperature differs by 0.7 K between the lower and upper RTD locations, which is significant when considering how the beams track across the aperture (Fig. 2). Depending on the scan angles, the temperature of the OBCT absorber seen by each band can vary by this amount and should be compensated for. Furthermore, the difference between the simulated RTD temperature and the absorber surface temperature introduces another error during calibration. For any value of z, the vertical offset between the dotted and solid line expresses the maximum temperature difference at that height. The temperature offset between the RTD location and the metal/absorber interface is an error independent of frequency because it occurs through the aluminum. Since the thickness of the metal is minimal at RTD location, the offset is low for all RTD positions at 0.01 K. The offset from the interface to the absorber skin increases along the height of the OBCT, starting with a negligible difference (< 0.01 K) at the lower RTD location, close to the wedge apex. For higher RTD locations, the gradient is 0.05 K for both RTD positions. The temperature gradient along this offset is linear. Compared with the vertical gradient across the wedge, the error between the RTD and surface temperature is negligible on the whole. However, the offset becomes significant close to the wedge aperture, exceeding 0.25 K.

V. Discussion

While the simulated scenario has not been replicated during testing, other tests in a laboratory atmosphere show a gradient of 0.6 K between the bottom and top of the wedge. During thermal cycling in vacuum (TVAC), the recorded wedge gradients were around 0.3 K, with a more homogeneous temperature environment than simulated. When using the data presented in Fig. 3 and focusing on the readings taken inside the OBCT aperture (coupling $\geq$ 99%), a temperature gradient is apparent for higher frequencies. Fig. 14 shows a zoomed-in plot where only the samples inside the OBCT aperture are considered. The gray area represents the temperature spread of the OBCT's RTDs. For the 54-GHz band, there is no variation, but considering the large beam size covering more of the wedge, combined with the large

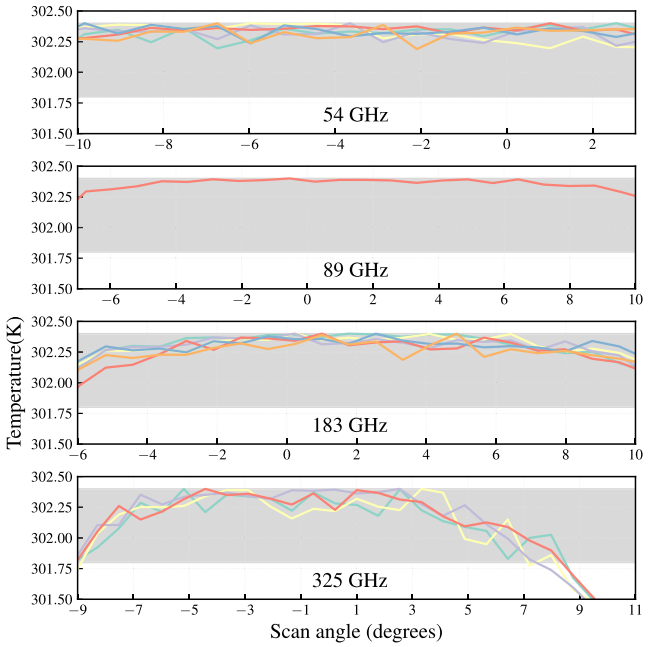

Fig. 14. Measured brightness temperatures for each band across OBCT aperture. Gray area denotes temperature range measured by OBCT sensors.

skin depth meaning absorption of the transmitted wave occurs across many reflections, this is expected. The gradient becomes more apparent with the increase in frequency and decrease in beam size, consistent with the two aforementioned factors. The 325-GHz band exceeds the measured temperature range for scan angles +9 to +11° off zenith. When considering RTD accuracy, how high these measurements sit in the wedge (Fig. 2), and the large delta between surface temperature and RTD measurement at those heights, it can explain this deviation. To avoid large calibration errors, it is advisable to disregard the measurements high up the wedge and restrict the scan range to a ±5° range around the apex of the wedge. As these measurements are not calibrated properly, but scaled according to the highest temperature measured in the OBCT, the absolute brightness temperatures shown here will not be accurate. However, it shows that the relative variations are realistic and demonstrate the effects discussed in this article. If the vertical gradient during operation is sufficiently low, e.g. less than 0.2 K, combined with the uncertainty of the RTDs (±0.15 K) it may be acceptable to use the OBCT without any further corrections of the effective brightness temperature. If the vertical gradient in operation is closer to the worst case thermal simulation of 0.7 K, it is possible to combine the GRASP simulations with the calculations of transmission and skin depth to build a ray tracing model of the OBCT and generate a weighting table for the RTDs which is frequency- and scan-angle-dependent. A further improvement is to more accurately calibrate the RTDs, reducing their uncertainty.

VI. Conclusion

The AWS OBCT consists of a wedge-shaped nonmagnetic absorber. The absorber is a three-part epoxy mixture cast onto an aluminum structure. The three parts are Stycast 1266,

carbon black powder, and boron nitride. Permittivity measurements at 26–40 GHz were used to simulate performance across the AWS bands for different thicknesses of a wedge with a 24° opening angle. Subsequent measurements of the finished OBCT showed a return loss better than 50 dB for TM mode, as predicted. As the beams are not co-aligned in the quasi-optics of the AWS radiometer, each frequency band couples differently into the OBCT aperture. Simulations using GRASP showed that the scan range of the primary mirror over which the coupling into the OBCT is greater than 99% is different for each band. Second, due to the varying beam sizes and their divergence from the primary mirror boresight, each band illuminates different parts of the OBCT aperture for a given scan angle. Furthermore, skin depth calculations for each band show that for the lowest three frequency channels, one reflection is not sufficient to absorb 99% of the transmitted energy. If the OBCT was homogeneous in temperature, this would not affect the calibration, but thermal simulations show that this is not the case. In the worst case scenario presented in this article, a temperature gradient of 0.7 K between the apex and the aperture of the OBCT is predicted, but data from TVAC testing show smaller gradients closer to 0.3 K. Horizontal temperature gradients between the RTD and the absorber skin are negligible for the majority of the wedge, but do become significant near the wedge aperture. Measurements taken from the AWS radiometer flight model confirm the anticipated effect of beam size and skin depth on the measured brightness temperature of the OBCT when a temperature gradient is present. Appropriate compensation for these effects will depend on the temperature gradient measured during in-orbit operation.

ACKNOWLEDGMENT

The authors would like thank Kalle Kempe from AAC Omnisys for providing test data from AWS PFM. They would also like to thank Daniele Piazza, Mathias Brändli, and Martin Rieder for the mechanical design of OBCT.

REFERENCES

[1] A. Schröder et al., "Electromagnetic design of calibration targets for MetOp-SG microwave instruments," *IEEE Trans. Terahertz Sci. Technol.*, vol. 7, no. 6, pp. 677–685, Nov. 2017.

[2] Q. Liu and J. A. S. S. Team, "Joint Polar Satellite System (JPSS) advanced technology microwave sounder (ATMS) SDR calibration algorithm theoretical basis document (ATBD)," Center Satell. Appl. Res., College Park, MD, USA, Tech. Rep. D0001-M01-S01-001_JPSS_ATBD_ATMS_SDR_B, 2022.

[3] H. Yang et al., "The FengYun-3 microwave radiation imager on-orbit verification," *IEEE Trans. Geosci. Remote Sens.*, vol. 49, no. 11, pp. 4552–4560, Nov. 2011.

[4] K. Jacob, A. Schroder, M. Kotiranta, and A. Murk, "Design of the calibration target for SWI on JUICE," in *Proc. 41st Int. Conf. Infr., Millim., Terahertz Waves (IRMMW-THz)*, Sep. 2016, pp. 1–2.

[5] R. V. Leslie, W. J. Blackwell, A. Cunningham, M. DiLiberto, J. Eshbaugh, and I. Osaretin, "Pre-launch calibration of the nasa tropics constellation mission," in *Proc. IEEE Int. Geosci. Remote Sens. Symp.*, Sep. 2020, pp. 6441–6444.

[6] S. Padmanabhan et al., "TEMPEST-D radiometer: Instrument description and prelaunch calibration," *IEEE Trans. Geosci. Remote Sens.*, vol. 59, no. 12, pp. 10213–10226, Dec. 2021.

[7] EUMETSAT. (2024). *Towards EPS-Sterna*. Brochure: PRG. FS.03, V1. [Online]. Available: https://www.eumetsat.int/media/51305

[8] R. Albers, A. Emrich, and A. Murk, "Antenna design for the Arctic weather satellite microwave sounder," *IEEE Open J. Antennas Propag.*, vol. 4, pp. 686–694, 2023.

[9] K. Jacob, A. Schröder, and A. Murk, "Design, manufacturing, and characterization of conical blackbody targets with optimized profile," *IEEE Trans. Terahertz Sci. Technol.*, vol. 8, no. 1, pp. 76–84, Jan. 2018.

[10] R. F. Harrington, *Time-Harmonic Electromagnetic Fields*. Hoboken, NJ, USA: Wiley-IEEE Press, 2001.

[11] J. Baker-Jarvis, *Transmission/Reflection and Short-Circuit Line Permittivity Measurements*. Gaithersburg, MD, USA: National Institute of Standards and Technology, 1990.

[12] F. Ulaby et al., *Microwave Radar and Radiometric Remote Sensing Sensing*. Ann Arbor, MI, USA: Univ. of Michigan Press, 2014, ch. 2–4, pp. 46–47.

[13] (2023). *Table of Emissivity of Various Surfaces*. Transmetra Gmbh. [Online]. Available: https://www.transmetra.ch/images/transmetra_pdf/publikationen_literatur/pyrometrie-thermografie/emissivity_table.pdf

Roland Albers received the B.Eng. degree in aerospace engineering with Brunel University London, London, U.K., in 2015, and the M.Sc. degree in astronautics and space engineering from Cranfield University, Milton Keynes, U.K., in 2016. He is currently pursuing the Ph.D. degree in applied physics with the University of Bern, Bern, Switzerland.

Before starting the Ph.D degree, he worked in the space industry on quasi-optical components. His research interests include spaceborne radiometry, hardware design, and calibration.

Tobias Plüss (Member, IEEE) received the M.Sc. degree in electrical engineering from the Lucerne School of Engineering and Architecture, Lucerne, Switzerland, in 2017.

During his B.Sc., he worked part-time at Siemens Switzerland, Zürich, Switzerland. From 2016 to 2018, he worked as an RF Electronics Engineer at Albis Technologies AG, Zürich. He joined the Institute of Applied Physics, University of Bern, Bern, Switzerland, in 2018. His research interests include design, simulation, and measurement of RF components, measurement of material parameters, network analyzer measurement techniques, and precise frequency and time measurement.

Lars Eggimann received the B.Sc. degree in physics from the University of Bern, Bern, Switzerland, in 2023, where he is currently pursuing the M.Sc. degree in experimental physics.

His research interests include numerical simulations and general application of computer science in physics.

Axel Murk received the M.Sc. degree in physics from the Technical University of Munich, Munich, Germany, in 1995, and the Ph.D. degree in physics from the University of Bern, Bern, Switzerland, in 1999.

Since then, he has been involved in the development and characterization of millimeter- and submillimeter-wave instrumentation for different ground-based and spaceborne projects. Since 2018, he has been leading the IAP Microwave Physics Division, University of Bern. His research interests include digital real-time spectrometers and radiometric calibration of remote sensing instruments.